



Chilean underground mine dataset

The International Journal of
Robotics Research
2017, Vol. 36(1) 16–23
© The Author(s) 2016
Reprints and permissions:
sagepub.co.uk/journalsPermissions.nav
DOI: 10.1177/0278364916679497
journals.sagepub.com/home/ijr



Keith Leung¹, Daniel Lühr³, Hamidreza Houshiar⁴, Felipe Inostroza², Dorit Borrmann⁴, Martin Adams², Andreas Nüchter⁴ and Javier Ruiz del Solar²

Abstract

This article presents a robotic dataset collected from the largest underground copper mine in the world. The sensor measurements from a 3D scanning lidar, a 2D radar, and stereo cameras were recorded from an approximately two kilometer traverse of a production-active tunnel. The equipment used and the data collection process is discussed in detail, along with the format of the data. This dataset is suitable for research in robotic navigation, as well as simultaneous localization and mapping. The download instructions are available at the following website <http://dataset.amtc.cl>.

Keywords

Field and service robotics, mapping, mining robotics, SLAM, robotics in hazardous fields, sensing and perception, computer vision, sensor fusion

1. Introduction

Located within the slopes of a volcano approximately 100 km south of Santiago, Chile, is the largest underground copper mine in the world. It consists of seven sectors of interconnected mines and we were granted a special permission to enter an active section of the mine, to collect a robotic dataset through a 2 km traverse. Due to the unique opportunity to access an active section of the underground mine with a robotic sensor suite, which has realistic variations in lighting, changes in terrain, elevation, and the presence of water, the dataset could be of interest to researchers in providing robust solutions to robotic navigation and simultaneous localization and mapping (SLAM) in challenging environmental conditions. Many other existing published datasets (Furgale et al., 2012; Peynot et al., 2010; Pomerleau et al., 2012; Tong et al., 2013), and openly accessible data (ASL, 2015; Bonarini et al., 2006; Magnusson et al., 2007; Nüchter and Lingemann, 2015) already provide an abundance of visual and lidar data. However, the particular location where the dataset was collected, along with the availability of the radar data makes this a unique dataset. The purpose of this paper is to describe the method in which the dataset was generated, as well as how it can be interpreted and accessed.

From a robotic mining perspective, this dataset is useful for the preliminary development and evaluation of autonomous vehicles for inspections of mines and caves, abandoned mine exploration, as well as smart mining and material exploitation, where the automated construction of

maps is necessary. From a more general robotic navigation and mapping perspective, this dataset is useful for the validation and the benchmarking of sensor fusion and SLAM systems in a realistic environment with variable illumination and surface properties, mainly due to the presence of water, uneven paths, and jagged walls. This dataset could also be used for studying continuous time estimation methods as some of the sensors operated at low-frequency cycles while the robot moved. Streams of information from individual sensors can be used independently to evaluate different types of algorithms such as visual odometry and point cloud registration.

The *Clearpath Robotics Husky A200* platform was used to carry the various on-board sensors, which include a stereo camera, a survey-grade 3D lidar, and a millimeter-wave radar. Figure 1 shows the sensor platform as it traversed a section of the tunnels that was relatively well illuminated. Some parts of the tunnels were dark and had a considerable amount of standing water, as well as water dripping from the ceilings, which makes this dataset challenging to process. For instance, visual-only navigation is

¹Applanix Corporation (Trimble Inc.), Canada

²Department of Electrical Engineering and the Advanced Mining Technology Center (AMTC), Universidad de Chile, Santiago, Chile

³Universidad Austral de Chile, Valdivia, Chile

⁴Julius-Maximilians-Universität, Würzburg, Germany

Corresponding author:

Keith Leung, Applanix Corporation (Trimble Inc.), 85 Leek Crescent, Richmond Hill, Ontario, L4B 3B3, Canada.
Email: kleung@applanix.com



Fig. 1. The Husky A200 robot platform carrying a stereo camera, 3D lidar, and a radar, as it traverses through a tunnel in the copper mine for dataset collection.

likely to fail in the parts of the tunnels without lighting, while standing water can reflect lidar beams.

The dataset was collected over a four-hour access window in the tunnels. It is available in both human-readable (text files and png images), as well as in a binary Robot Operating System (ROS) bag format containing standard ROS messages. For organizational purposes, the dataset has been sub-divided into 87 parts. Of the 87 parts, 44 of them were recorded while the robot was stationary at various locations inside the mine. Between the stationary measurement poses, the robot made 43 traverses during which data from various sensors was also recorded. Each of these traverses constitute one part of the dataset. These 43 parts, along with the 44 parts for performing the stationary measurements, make up the entirety of the dataset.

The remainder of this article is structured as follows. Section 2 describes in greater detail the robotic platform and the sensors used in collecting the dataset. Section 3 details the calibration and data collection process. Finally, Section 4 describes the format of the data and ways in which it can be accessed.

2. Equipment and sensors

2.1. Robot platform

The *Clearpath Robotics Husky A200* in Figure 1 was the vehicle used for collecting the dataset. It carried the stereo camera, 3D lidar, and radar on its upper sensor deck, while hosting extra batteries for powering the sensors and two on-board computers on its lower deck. The Husky is a skid-steer vehicle, and both left and right wheel encoder readings were recorded. The wheel-base distance between each pair of front and rear wheels is 50 cm.



Fig. 2. A pair of images from the stereo camera taken at the start of the dataset collection. In relation to Figure 6, the pose of the robot is located at point A, and directed at point B with its forward direction. A gate can be seen in the upper-left corner of both images. The bright orange spots in the upper-center of the images is a pool of water reflecting a set of ceiling-mounted warning lights. The darker spots on the ground are damp surfaces.

2.2. Stereo camera

A *Point Grey XB3* multi-baseline stereo camera was mounted near the front of the Husky A200, with a forward-facing orientation that is also downward-pitched at about 20 degrees to the horizontal plane of motion of the vehicle (see Section 3 for its precise pose). The wider 24 cm baseline configuration for the stereo camera was used. Synchronized left and right (global-shutter) camera images were captured at 16 Hz, both at a resolution of 1280×960 pixels per image. A pair of images from the stereo camera taken from the start of the dataset is shown in Figure 2. Note that in many images, light from headlamps can be observed. Due to safety regulations, they could not be turned off during dataset collection.

2.3. 3D lidar

A *Riegl VZ-400* survey-grade 3D lidar was mounted behind the stereo camera. This sensor has a quoted range limit of 350 m, with a range accuracy of 5 mm, and beam divergence of 0.3 mrad. It is capable of making 125,000 measurements per second. The generated point cloud contains both positional and intensity information. The intensity information is the relative reflectance in dB, which corresponds to the ratio of the amplitude of the return signal to the amplitude of a white flat (diffuse) target at the same distance and which is aligned orthogonal to the laser beam. Thus, a white target has a 0 dB as intensity (Riegl Laser Measurement Systems, 2009). A relative reflectance higher than 0 dB results from targets reflecting with a directivity different from that of a Lambertian reflector, such as a reflective marker being placed in the environment for surveying. Non-reflections are not reported in this dataset, but the direction (azimuth and elevation) of non-returns could potentially be estimated by first converting a scan into polar coordinates and then searching for the set of azimuth and elevations with the missing data. Scans were obtained at

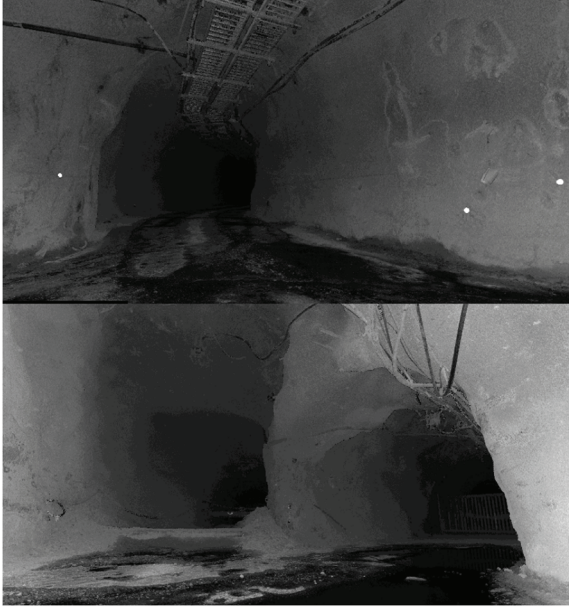


Fig. 3. High resolution point clouds which were logged from the Riegl lidar with high (whiter) pixel values corresponding to high reflectance. Pixel intensities are also attenuated exponentially with respect to the distance to the lidar. In relation to Figure 6, the top scan was collected at Point B, where some reflective markers can be seen (in bright white). These were used for evaluating the accuracy of the pose estimate provided in this dataset. The bottom scan was recorded at point E.

two different resolutions. When the Husky A200 was stationary, high resolution point clouds were recorded at vertical and horizontal resolutions of 0.04 degrees, and at a scan rate of one full scan per 152.5 s^{-1} . When the robot was moving between stationary scan positions, the lidar was commanded to rotate and scan continuously at a higher frequency of one (360 degree) rotation of the sensor every six seconds. This produced scans at lower vertical and horizontal resolutions of 1 degree. Two sample high resolution lidar point clouds which were taken while the robot was stationary are shown in Figure 3.

2.4. 2D radar

An AcuMine frequency-modulated continuous-wave high-speed millimetric (94 GHz) 2D radar (Brooker et al., 2005) was mounted near the rear of the Husky A200. The sensor was operated in a continuous scanning mode where the swashplate rotated at 1 Hz, with a radar sample rate of 435 Hz. Power return values were recorded every 0.5 m up to an operational range of 200 m, and at angular resolutions of 0.68 degrees. The antenna beam width is 1.5 degrees, and the beam is capable of penetrating small dust particles due to its relatively longer wavelength when compared to the lidar. An example of a (cropped) radar scan at a tunnel junction is shown in Figure 4. The origin of the sensor is located

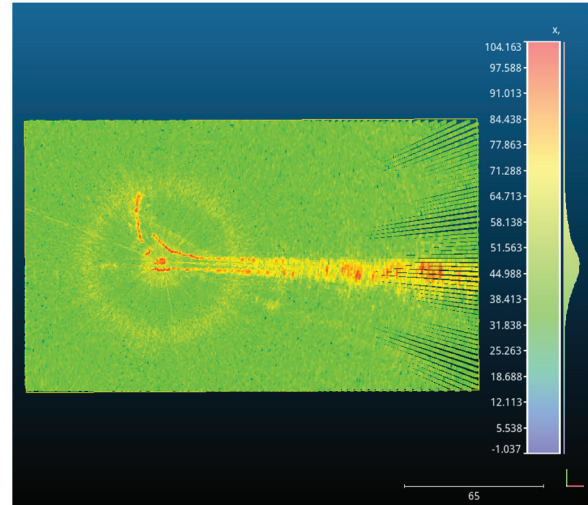


Fig. 4. A 2D radar scan from point B of Figure 6. The sensor is located towards the left side of the figure. The scale for power return values in dB is on the right. Higher power returns (from tunnel walls) are colored in red. A faint yellow halo centered about the sensor is caused by interference from the radar's power supply.

towards the left side of the figure. The faint yellow halo centered about the sensor is an artifact caused by interference from the power supply of the radar. An in-depth explanation of this phenomenon can be found in Adams et al. (2012). At several scan locations, radar data is not available due to hardware problems with the sensor. These locations have been noted in Table 1. Fortunately, due to the range of the sensor, sufficient overlaps exist between the collected radar data to cover the traversed tunnels.

3. Data collection

3.1. Calibration

Prior to the dataset collection, calibration parameters for the stereo camera, as well as the relative pose between each sensor reference frame was determined. These frames are illustrated in Figure 5, with the precise relative transformations reported in Table 2.

The base frame is centered between the four wheels of the Husky A200, with the x -axis aligned with the forward direction. The pose of the lidar frame is fixed by mechanical design. The translation between the lidar and radar frame is also determined by mechanical design, while the relative rotation was calculated by aligning the scans between the two sensors. For the lidar and the stereo camera, distinct tie points were manually selected from multiple sets of scans and images to calculate their relative transformation through least squares optimization. The intrinsic and extrinsic calibration parameters for the stereo camera were obtained by the standard checkerboard calibration process

Table 1. Data description.

Data sequence	Location (see Figure 6)	Notes
00S	Location A	This is the start of the dataset, with the robot facing towards point B. Radar information is not available.
01M, 01S	From A to B	Radar information is not available for 01M.
02M, 02S, . . . , 08S	From B to C	
09M, 09S, . . . , 11S	From C to D	The tunnel between 09S and 10S is dark, but light can be seen from the tunnel ahead.
12M, 12S, . . . , 14S	From D to E	The tunnel between 11S and 14S is dark and turns gradually. Light seen in the stereo camera images are from the safety headlamps of the operators. A large amount of standing and dripping water is present.
15M, 15S	Location E	Ahead of the robot at 15S is a shaft for depositing material that will fall into lower levels of the mine. Radar data is not available.
16M, 16S, . . . , 19S	From E to D	The tunnel is dark. Light seen in the stereo camera images are from the safety headlamps of the operators. A large amount of standing and dripping water is present. Radar data is not available for 16S and 17S.
20M, 20S, 21M, 21S	From D to C	The section traversed in 21M is initially dark. This is the same dark section between 09S and 10S but traversed in the reverse direction.
22M, 22S, . . . , 25S	From C to F	This section is an uphill ascent. The tunnel section between 22S and 24S is dark.
26M, 26S, . . . , 30S	From F to G	Radar data is not available from 28M to 30M.
31M, 31S, . . . , 33S	From G to B	This section is a downhill descent. At the end of 33M, the robot makes a u-turn and climbs slightly uphill towards point G before stopping.
34M, 34S, . . . , 35M	From B to G	This section is an up-hill ascent. Traverse 35M passes through point G without stopping.
35M, 35S, . . . , 37S	From G to F	
38M, 38S, . . . , 40S	From F to C	This section is a downhill descent. Traverse 38M is mostly a dark section of the tunnel that corresponds to the dark section experienced between 22S and 24S. At the end of traverse 40M, the robot turns at junction C to face the direction of junction B.
41M, 41S, . . . , 43S	From C to B	The dataset ends with the robot at point B

(Zhang, 2000). Specifically, the calibration pipeline implementation in OpenCV (Bradski et al., 2000) was used to obtain the camera parameters in Table 3, which assumes the Brown–Conrady distortion model (Brown, 1966).

3.2. Data recording

Two computers were installed on-board the Husky A200 for dataset collection. The first computer, dedicated to data logging, was connected to the Husky’s communication port for controlling the motion of the vehicle and receiving wheel

encoder measurements. This computer was also connected to the stereo camera and the lidar. The second computer was a dedicated radar server, and all radar measurements were relayed to the first computer for logging.

Throughout the four-hour traverse, the Husky stopped at 44 locations (including the starting position) to record high resolution 3D lidar point clouds, each of about 25 million points, while the robot remained stationary. In straight tunnel sections, the distances between the stopped locations was between approximately 30 m and 40 m to obtain sufficient overlap between the consecutively obtained point

Table 2. The relative transformations between sensor reference frames. The rotation brings a point in frame (b) into frame (a), and the translation is defined from frame (b) to frame (a) with respect to the coordinates defined in frame (a).

Frames		Rotation (quaternion) $\mathbf{q}_{a,b} = [q_x \ q_y \ q_z \ q_w]$
(a)	(b)	Translation (m) $\mathbf{p}_a^{b,a} = [p_x \ p_y \ p_z]$
base	lidar	$\mathbf{q}_{a,b} = [0 \ 0 \ 1 \ 0]$ $\mathbf{p}_a^{b,a} = [0.120 \ -0.003 \ 0.840]$
lidar	radar	$\mathbf{q}_{a,b} = [0 \ 0 \ 0.707 \ 0.707]$ $\mathbf{p}_a^{b,a} = [0.292 \ -0.003 \ 0.401]$
lidar	stereo left	$\mathbf{q}_{a,b} = [0.584 \ 0.573 \ -0.407 \ -0.407]$ $\mathbf{p}_a^{b,a} = [-0.164 \ -0.106 \ -0.152]$
stereo left	stereo right	$\mathbf{q}_{a,b} = [0 \ 0 \ 0 \ 1]$ $\mathbf{p}_a^{b,a} = [0.240 \ 0 \ 0]$

clouds. These distances were increased when the robot was in a section that it has previously traversed. Radar measurements were also logged when the robot was stationary, but the stereo camera images and the wheel encoder readings were not.

Between the stationary scan poses, 43 traverses were conducted by manually controlling the robot. During each traverse, measurements from the wheel encoders, lidar, radar, and stereo camera were logged. The lidar was configured to scan at a lower resolution to increase the scanning frequency while the robot was moving.

3.3. Time synchronization

A *Network Time Protocol* (NTP) daemon was used to synchronize the clocks between the two on-board computers. The first computer, dedicated to data logging, was setup as the NTP server, while the radar server computer was the NTP client. Sufficient time was allowed after booting up both of the computers so that the client clock could adjust. The average time difference is on the order of 10^{-3} s. Measurements from the wheel encoders, lidar, and stereo camera were time-stamped using the data logging computer's clock, while radar measurements were time-stamped using the radar server's clock.

3.4. Scan pose estimates by supervised pointcloud alignment

The tunnel environment made obtaining the ground-truth robot poses a challenging task due to both occlusions and the aspect ratio of the long and narrow tunnels. Reflective markers were placed at tunnel junctions, but it was infeasible to cover all the traversed tunnels with markers. Since the Riegl is a survey-grade lidar, and the most accurate sensor available on the robot, the pose estimates of the robot at the 44 static scan positions were determined by using the high-resolution 3D point clouds from the lidar. Manual alignment was performed on the consecutive 3D point clouds from the 44 static scanning positions. The batch optimization method in Borrmann et al. (2008) for pose-graph relaxation is then used to refine the alignment², and was used to generate Figure 6. The positional errors of the reflective markers, of 50 mm diameter which were observed from various poses, were used to evaluate the quality of the solution, which is a common practice in surveying. The average marker position error between scan pairs is

Table 3. Stereo camera calibration parameters, assuming the Brown–Conrady distortion model (Brown, 1966).

Parameter	Left camera	Right camera
Tangential distortion \mathbf{p}	$p_1 = 0.000571 \quad p_2 = 0.000539$	$p_1 = 0.000959 \quad p_2 = 0.000514$
Radial distortion \mathbf{k}	$k_1 = -0.177067 \quad k_2 = -0.165155 \quad k_3 = -0.142561$ $k_4 = 0.192250 \quad k_5 = -0.316417 \quad k_6 = -0.196546$	$k_1 = 0.746517 \quad k_2 = -0.321874 \quad k_3 = -0.788330$ $k_4 = 1.099655 \quad k_5 = -0.043691 \quad k_6 = -1.203787$
Rectification matrix \mathbf{R}	$\begin{bmatrix} 0.999997 & -0.002331 & -0.001186 \\ 0.002327 & 0.999992 & -0.003369 \\ 0.001194 & 0.003366 & 0.999994 \end{bmatrix}$	$\begin{bmatrix} 0.999993 & -0.003561 & 0.001203 \\ 0.003557 & 0.999988 & 0.003370 \\ -0.001215 & -0.003365 & 0.999994 \end{bmatrix}$
Projection matrix \mathbf{P}	$\begin{bmatrix} 997.177459 & 0.000000 & 667.571815 & 0.000000 \\ 0.000000 & 997.177459 & 496.314240 & 0.000000 \\ 0.000000 & 0.000000 & 1.000000 & 0.000000 \end{bmatrix}$	$\begin{bmatrix} 997.177459 & 0.000000 & 667.571815 & -239.608595 \\ 0.000000 & 997.177459 & 496.314240 & 0.000000 \\ 0.000000 & 0.000000 & 1.000000 & 0.000000 \end{bmatrix}$

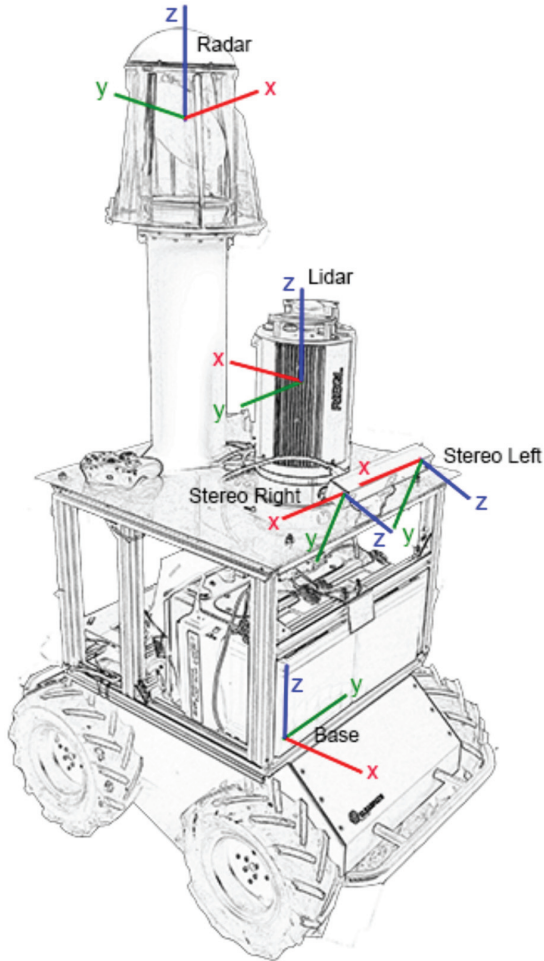


Fig. 5. Sensor reference frames used in the dataset. The base frame in which odometric data is expressed is centered between the four wheels of the Husky. The x , y , and z axes are colored in red, green, and blue, respectively. The precise transformations between the sensor frames are listed in Table 2.

10.41 mm, with the standard deviation being 8.25 mm, and the maximum error being 32.34 mm. The top-view map shown in Figure 6 was constructed based upon all the point clouds being plotted with the 44 pose estimates. Figure 7 shows the alignment between two overlapping point clouds.

3.5. The traverse

With reference to Figure 6, the approximately two-kilometer traverse started at point A, and then proceeded to the tunnel junction at point B. Next, the Husky traversed to the tunnel junction at point C, and continued on to point E through point D. In the vicinity of point D, there was no lighting in the tunnel, and there was a significant amount of standing water, as well as water dripping from the ceiling. Point E is a material drop point, from here the robot turned around and returned to the junction at point C. A right turn was then made to point F, where again there was a lack of lighting. The robot continued to the junction at

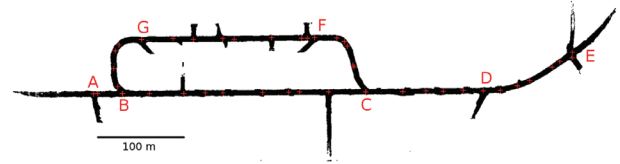


Fig. 6. A view of the map generated from the 3D point clouds at each of the estimated scan poses. Various points of interests are labeled. The data collection traverse initiated at point A and continued to points B, C, D, E, D, C, F, G, B, G, F, C, and finally returned to point B at the end of the dataset. Stationary scan points are marked as crosses.

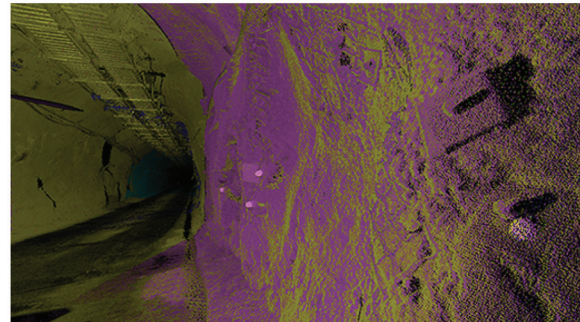


Fig. 7. Two overlapping point clouds shown in different colors, showing the quality of the scan pose estimation method.

point B through point G, and then turned around to retrace its path to point C through points G and F. At the junction at point C, the robot turned right, and then returned to the junction at point B.

4. Data format and usage

The dataset is divided into 87 parts. The data is provided in human-readable text files and png images. The same data is also available as ROS bag files for convenience. For the human-readable files, the following is a description of their file naming convention and their content. Note that each data file also contains a one-line header that describes the columns of the data.

4.1. File naming convention

All of the files with logged sensor data have names that start with a double digit scan index. The letter following the scan index is either an “S” or “M”, and denotes whether the data was gathered when the robot was stationary, or while the robot was moving between stationary scan points, respectively. The data gathered while the robot was stationary are indexed separately from the data gathered while the robot was moving. The data files from the first stationary logging position are indexed with “00”, while the data from the first traverse are indexed with “01”. Hence, the dataset was collected in the sequence 00S, 01M, 01S, 02M, ..., 43M, 43S.

The approximate topological position of the robot in relation to Figure 6, along with notes of interest, are provided in Table 1 for each sub-part. Following this alpha-numeric index is a string identifying the type of data that the file contains. This string can be “_encoder”, “_stereo”, “_lidar”, “_radar” or “_timing”. The names of all text files end with “.dat”, while for stereo image files, the data type string “_stereo” is followed by “_”, a six digit integer for the image sequence, “L” or “R” for the left or right camera, and a “.png” file extension. The contents of the text files will be described next.

4.2. Wheel encoder file

Each line of an encoder file contains

$$[\text{time}] \quad [\text{enc}_{\text{left}}] \quad [\text{enc}_{\text{right}}]$$

where the time-stamp is in seconds, and enc_{left} and $\text{enc}_{\text{right}}$ are the left and right encoder data, respectively, expressed as distance traveled in meters.

Dead-reckoning estimates from the encoders can be inaccurate due to the skid-steer mechanics of the Husky, as well as the wet, slippery ground surface within the mine tunnels.

4.3. Stereo images

Text files `##X_stereo.dat` contain the time-stamp information for each indexed image pair. Each line in these files is in the following format

$$[\text{time}] \quad [\text{index}]$$

where the time-stamp is in seconds and the index is a six-digit integer that corresponds to the index used in the file names of the stereo image .png files.

4.4. Lidar point cloud file

Each line in a lidar data file represents one point and is recorded in the format

$$[\text{time}] \quad [x] \quad [y] \quad [z] \quad [i]$$

where the time-stamp is in seconds, followed by the x, y, z 3D coordinate of a point in the lidar reference frame, and its intensity, i , in dB. The center of the lidar is positioned at $(0, 0, 0)$.

4.5. Radar file

A line in a radar data file corresponds to a scan sector (a particular angle of the radar swashplate, and range bin), and has the following format

$$[\text{time}] \quad [x] \quad [y] \quad [p]$$

where the time-stamp is in seconds, followed by x, y , the 2D coordinate representing the center of a received-signal bin (from the discretized measurement space). The last field, p , is the received power in dB.

4.6. Timing file

The timing information from all sensor messages are summarized in the `##X_timing.dat` files. This is to facilitate the reading of sensor messages from their respective data files in the proper order. Each line in a timing file is in the following format

$$[\text{time}] \quad [S]$$

where the time-stamp is in seconds, and S is a letter representing the sensor message. This can be W for the wheel encoder, C for stereo camera, L for lidar, or R for radar.

4.7. Sensor pose file

The relative transformation between the sensor frames of Table 2 are written in the `frames.dat` file. A transformation that brings a point to frame a from frame b using a rotation quaternion $\mathbf{q}_{a,b} = [q_x \ q_y \ q_z \ q_w]$ and translation vector $\mathbf{p}_a^{b,a} = [p_x \ p_y \ p_z]$ in units of m is written in two lines in the following format

$$\begin{array}{l} [\text{frame } a] \quad [\text{frame } b] \\ [q_x] \quad [q_y] \quad [q_z] \quad [q_w] \quad [p_x] \quad [p_y] \quad [p_z] \end{array}$$

4.8. Camera calibration file

The file `camera.dat` contains eight lines, with the first four lines containing rectification information for the left stereo camera, and the last four for the right stereo camera. Each set of four lines lists, in order, the tangential distortion parameters, radial distortion parameters, the rectification matrix, and the projection matrix (both in row-major order). The following are the lines corresponding to the left camera

$$\begin{array}{l} p_1 \quad [p_1] \quad [p_2] \\ k_1 \quad [r_1] \quad [r_2] \quad \dots \quad [r_6] \\ R_1 \quad [\mathbf{R}_{1,1}] \quad [\mathbf{R}_{1,2}] \quad \dots \quad [\mathbf{R}_{3,3}] \\ P_1 \quad [\mathbf{P}_{1,1}] \quad [\mathbf{P}_{1,2}] \quad \dots \quad [\mathbf{P}_{4,4}] \end{array}$$

4.9. Estimated pose file

Estimates for the 44 stationary scan poses are recorded in the file `scanPoseEstimates.dat`. Each line begins with the data sequence identification (e.g. 00S for the first stationary data collection pose), followed by its position and orientation (expressed as a rotation quaternion) relative to the first stationary data collection pose

$$[\text{sequence}] \quad [q_x] \quad [q_y] \quad [q_z] \quad [q_w] \quad [p_x] \quad [p_y] \quad [p_z]$$

4.10. Access

Instructions for downloading the dataset are available at the website <http://dataset.amtc.cl>.

Acknowledgments

The authors acknowledge Paul Vallejos and Rodrigo Asenjo from the Advanced Mining Technology Center (AMTC) for facilitating

the logistics that made the dataset collection possible. The authors also gratefully acknowledge the Julius–Maximilians-Universität Würzburg, Germany for their provision of the Riegl 3D lidar.

Funding

The author(s) disclosed receipt of the following financial support for the research, authorship, and/or publication of this article: This work was funded by the Conicyt-DAAD collaborative project PCCI12009 and Fondecyt projects 1150930 and 3150066. The Husky A200 robotic platform was partially supported by the Clearpath Robotics “Partnerbot” program, with the remaining cost of the robot and other sensors being funded by the Universidad de Chile. The support of the AMTC is also acknowledged.

Notes

1. See 2009 Riegl Laser Measurement Systems “Riegl vz-400” data sheet
2. The source code for this method is part of the 3D Toolkit, and is available for download at <http://slam6d.sourceforge.net>.

References

- Adams M, Mullane J, Jose E, et al. (2012) *Robotic Navigation and Mapping With Radar*. USA: Artech House.
- ASL (2015) ASL datasets repository. Available at: <http://projects.asl.ethz.ch/datasets> (accessed 24 August 2016).
- Bonarini A, Burgard W, Fontana G, et al. (2006) Rawseeds: Robotics advancement through web-publishing of sensorial and elaborated extensive data sets. In: *Proceedings of IROS workshop on benchmarks in robotics research*, Beijing, China, 2006. USA: IEEE.
- Borrmann D, Elseberg J, Lingemann K, et al. (2008) Globally consistent 3d mapping with scan matching. *Robotics and Autonomous Systems* 56(2): 130–142.
- Bradski G (2000) The opencv library. *Dr. Dobbs Journal of Software Tools* 25(11): 120–126.
- Brooker GM, Scheduling S, Bishop MV, et al. (2005) Development and application of millimeter wave radar sensors for underground mining. *Sensors Journal* 5(6): 1270–1280.
- Brown DC (1966) Decentering distortion of lenses. *Photometric Engineering* 32(3): 444–462.
- Furgale PT, Carle P, Enright J, et al. (2012) The Devon island rover navigation dataset. *The International Journal of Robotics Research* 31(6): 707–713.
- Magnusson M, Duckett T and Lilienthal AJ (2007) Scan registration for autonomous mining vehicles using 3D-NDT. *Journal of Field Robotics* 24(10): 803–827.
- Nüchter A and Lingemann K (2015) 3D robotic scan repository. Available at: <http://kos.informatik.uni-osnabrueck.de/3Dscans/> (accessed 24 August 2016).
- Peynot T, Scheduling S and Terho S (2010) The marulan data sets: Multi-sensor perception in a natural environment with challenging conditions. *The International Journal of Robotics Research* 29(13): 1602–1607.
- Pomerleau F, Liu M, Colas F, et al. (2012) Challenging data sets for point cloud registration algorithms. *The International Journal of Robotics Research* 31(14): 1705–1711.
- Riegl Laser Measurement Systems (2009) RiSCAN PRO. Software Description & User’s Instruction. Version 1-5-0sp1.
- Tong C, Gingras D, Larose K, et al. (2013) The Canadian planetary emulation terrain 3d mapping dataset. *The International Journal of Robotics Research* 32(4): 389–395.
- Zhang Z (2000) A flexible new technique for camera calibration. *Pattern Analysis and Machine Intelligence, IEEE Transactions on* 22(11): 1330–1334.